



Experimental and Computational Analysis of Slurry-Based Manufacturing of Solid-State Battery Composite Cathode

Mohammed Alabdali,^[a, b] Franco M. Zanotto,^[a, b] Benoît Notredame,^[c] Virginie Viallet,^[a, b] Vincent Seznec,^[a, b, d] and Alejandro A. Franco^{*[a, b, d, e]}

The rheological properties of the slurry significantly influence the manufacturing process of solid-state battery cathode electrodes, affecting coating quality and the resulting cathode microstructure. The correlation between slurry attributes and final electrode characteristics is analyzed using particle size and solid content as key metrics. We perform coarse-grained molecular dynamics simulations of $\text{LiNi}_{0.8}\text{Mn}_{0.1}\text{Co}_{0.1}\text{O}_2$ and $\text{Li}_6\text{PS}_5\text{Cl}$ composite electrodes, with simulated slurries closely fitting experimental viscosities, indicating the model's suitability for predicting slurry behavior. Then the microstructural properties of the dried and calendered electrodes are calibrated with *in house* experimental data. The simulation workflow is fitted completely using only two sets of force fields, one for the slurry

and the other one for the dried state of the electrode. The effective electronic conductivities are contingent on the particle size, without showing significant limitation on cathode power capabilities. This comprehensive study highlights the intricate interplay between slurry solid content, microstructure design, and manufacturing processes in optimizing solid-state battery cell performance. Consistent slurry characteristics are crucial for uniform electrode coating while optimizing particle size and solid content improves electrode porosity. These findings provide valuable insights for enhancing solid-state battery electrode design and slurry-based manufacturing processes for the adaptation of already established scaling up technologies.

1. Introduction

Solid-state batteries (SSBs) hold immense promise for revolutionizing energy storage due to their potential for high theoretical energy densities.^[1] This technology offers potential advantages over traditional lithium ion batteries (LIBs) depending on the SSB design, including enhanced current density, faster charging rates, a wider operational voltage window, and improved safety – characteristics that are particularly attractive for electric vehicles and other demanding applications.^[2]

However, a key challenge in developing high-performance SSBs lies in achieving a balance between maximizing energy density and enabling fast charging rates within composite electrodes. High energy density is achieved by incorporating a high-volume fraction of energy-dense active materials (AM) in

the composite electrode. This creates impeded electronic conductive pathways, so carbon additives are incorporated to enhance the electronic conductivity. However, a high AM fraction also reduces the volume available for the solid electrolyte (SE), hindering ion transport pathways. From an energy density perspective, the presence of SE in the cathode is not desirable because it displaces the high-density, chemically active AM particles. Additionally, certain SEs, such as oxides or halides, add significant weight to the cell.^[2,3]

On the other hand, fast charging necessitates a well-connected network of SE for rapid ion transport. Effective SE integration in SSB electrodes and cells requires the material to satisfy specific chemical and mechanical criteria. Physically, the SE should exhibit minimal electronic conductivity, high ionic conductivity, as well as excellent electrochemical compatibility with the other cell components. Mechanically, the SE needs adequate stiffness and fracture toughness to maintain structural integrity during battery cell operation. Recent research has made significant progress in addressing sluggish ionic conductivity, a major hurdle in incorporating SEs into next-generation battery designs.^[4–6] Striking a balance between these competing demands in terms of electrochemical performance and mechanical requirements is crucial for the successful development of high-performance SSB composite cathodes.^[7–10]

These electrodes comprise a densely packed microstructure of AM particles surrounded by a conductive SE network for ionic transport, often with additional conductive additives. During lithium ion (de)intercalation, the AM particles undergo volumetric expansion and contraction. This volume change within the confined SSB cell architecture can generate significant stresses.^[11,12] The rigid solid framework transmits these stresses, leading to a complex coupled chemo-mechanical

[a] M. Alabdali, F. M. Zanotto, V. Viallet, V. Seznec, A. A. Franco
Laboratoire de Réactivité et Chimie des Solides (LRCS), Université de Picardie Jules Verne, Hub de l'Energie, UMR CNRS 7314, 15 rue Baudelocque, 80039 Amiens, France
E-mail: alejandro.franco@u-picardie.fr

[b] M. Alabdali, F. M. Zanotto, V. Viallet, V. Seznec, A. A. Franco
Réseau sur le Stockage Electrochimique de l'Energie (RS2E), Hub de l'Energie, FR CNRS 3459, 15 rue Baudelocque, 80039 Amiens, France

[c] B. Notredame
Umicore, 31 rue Marais, 1000 Brussels 8, Belgium

[d] V. Seznec, A. A. Franco
ALISTORE-European Research Institute, Hub de l'Energie, FR CNRS 3104, 15 rue Baudelocque, 80039 Amiens, France

[e] A. A. Franco
Institut Universitaire de France, 103 boulevard Saint Michel, Paris 75005, France

Supporting information for this article is available on the WWW under <https://doi.org/10.1002/batt.202400709>

response that can cause damage within the AM particles, the SE itself, or at the interface between the two. Addressing these mechanical challenges is essential for creating robust composite cathodes in SSBs,^[3] where $\text{LiNi}_x\text{Mn}_y\text{Co}_{(1-x-y)}\text{O}_2$ (NMC) is a promising AM candidate for next-generation battery technologies due to its high theoretical capacity, energy density, structural stability, and inherent rate capability.^[2] However, scaling up the production of SSB electrodes and cells is crucial for commercial viability. Electrode microstructure design plays a critical role in achieving high-performance SSBs when scaling up NMC-based battery technology.^[12–16]

Despite significant interest, the scaling-up of SSB electrode solvent-based manufacturing has only been achieved by the private sector whose expertise remains unpublished and has not been sufficiently covered in literature, as most studies focus on dry processing.^[17–19] Ates *et al.*^[20] deliver a scalable slurry-based production method for SSB electrodes, focusing on one composition for the composite cathode. Their solid-state cell exhibits acceptable cycle performance and specific capacity, with conductive carbon being critical to performance. This study only explores one set of production parameters (e.g. same conditions of the preparation of the composite electrode, solid electrolyte layer and solid polymer electrolyte layer) and operating conditions (e.g. cycling at 60 °C and C/20 c-rate), yet highlights a promising approach toward the commercial viability of SSBs.

Uniform slurry casting depends on several factors, including solvent, binder, solid content, and formulation. An optimized LIB cathode electrode slurry typically contains over 95% AM with N-methylpyrrolidone (1.89 mPa·s viscosity at 25 °C) as the solvent and 70% solid content, achieving a viscosity of 1.0–2.0 Pa·s for smooth casting.^[14] In contrast, a SSB electrode slurry composition is typically less optimized, with 64% AM, 30% SE, and Butyl acetate (0.69 mPa·s viscosity at 25 °C) as the solvent, along with 50% solid content, resulting in a much lower viscosity range of 0.1–0.3 Pa·s – about an order of magnitude lower than that of the LIB case. To avoid the necessity of building entirely new plants for SSB cells production, it is essential to qualify and adapt current manufacturing technologies to accommodate the properties of SSB electrode materials and the requirements of novel components. The feasibility of the slurry-based processing method for SSB cathodes has been demonstrated at the laboratory scale.^[20–23] Singer *et al.*^[23] investigated the viability of various conditions for slurry-based processes in the production of sulfide-based SSB composite cathodes. The study examined how binder and solid content in the slurry impact viscosities, sheet thicknesses, and areal weights. Additionally, they demonstrated using thickness variation over the geometric area how material properties can be adjusted to achieve high throughput in pilot-scale coating processes. However, many aspects of large-scale fabrication remain unknown.^[24–26]

3D physical models^[24,25] of LIB electrode manufacturing have demonstrated a commendable compromise between throughput and accuracy. However, the existant modeling literature on SSBs is comparatively limited,^[13] with scant studies focusing on manufacturing. LIB physics-based 3D models afford precise

control over each manufacturing parameter, enabling a robust capability to comprehend and scrutinize manufacturing effects on the electrode's microstructure. We have devised a series of SSB and LIB models ascribed to distinct steps of the manufacturing process, commencing from the slurry phase,^[26] through drying,^[27,28] and electrode calendering.^[28,29] The culmination of this model chain can be seamlessly integrated into 4D (3 geometrical dimensions + dimension of time) electrochemical models to simulate energy discharge^[30] and electrochemical impedance spectroscopy (EIS).^[31] As a result, this approach is able to link manufacturing conditions, microstructure, and performance. The ultimate goal is to be able to predict experimental discharge-recharge profiles of electrodes, in half- or full cells, generated according to a particular set of manufacturing parameters. This study explores for the first time a dual experimental and modeling approach to investigate multiple slurry-based manufacturing parameters' influence on SSB cathode characteristics.

Materials and Methods

Experiments

Preparation of Electrode Composites

Cathode composites were prepared by mixing 64 wt.% of single-crystalline $\text{LiNi}_{0.8}\text{Mn}_{0.1}\text{Co}_{0.1}\text{O}_2$ (NMC811, Umicore) as AM, 30 wt.% of $\text{Li}_6\text{PS}_5\text{Cl}$ (Umicore) as SE and 3 wt.% of carbon additives (SuperP, Imerys) as the dry cathode mixture. Two different particle size distributions (PSDs) of the AM used are shown in Figure S3 in the Supplementary Information (SI) and the electrodes thus formed are referred to hereafter as AM_1 and AM_2 where their volumetric D_{50} 's are 4 μm and 6 μm, respectively (D_{50} being the median diameter of the particles). The mean particle sizes of the SE and the SuperP carbon particles were 1 μm and 40 nm, respectively. The PSDs were measured by laser diffraction and provided by our industrial supplier (Umicore) and the exact PSDs cannot be disclosed due to Umicore's confidentiality. All components were transferred into a 12 mL plastic cup with two zirconia spheres (1 mm in diameter) and dry mixed using a planetary mixer with a rotation speed of 2000 rpm for 4 min.

A binder-solvent solution was prepared by adding 5 wt.% of polyvinylidene fluoride as binder into 95 wt.% of anhydrous butyl acetate, since $\text{Li}_6\text{PS}_5\text{Cl}$ is not soluble in nonpolar solvents, and then mixed at 500 rpm for overnight to ensure the binder was well dissolved in the solvent. To prepare the electrode slurry, 3 wt.% of the targeted dried electrode composition was calculated, and the corresponding amount of binder-solvent solution was added to the plastic cup containing the dry cathode mixture with different amounts of solvent to reach the respective solid content (SC) of 48%, 50% and 52%. The slurry was then mixed in the planetary mixer at 2000 rpm for 7 min. After completion, the slurries were then casted on Al foil using a doctor blade with a 100 μm comma gap for AM_1 and 300 μm comma gap for AM_2 , as the AM_2 resulted in mechanically unstable homogenously thin electrodes. With pressing, these electrodes do not prevent the two current collectors to come in contact and the short circuit when casted with 100 μm doctor blade. The casted electrodes (Figure 1) were dried in a vacuumed oven at 60 °C for overnight. All materials used were already dried and all procedures were handled at Umicore's dry room with a dew point of $-69 \pm 2^\circ\text{C}$.

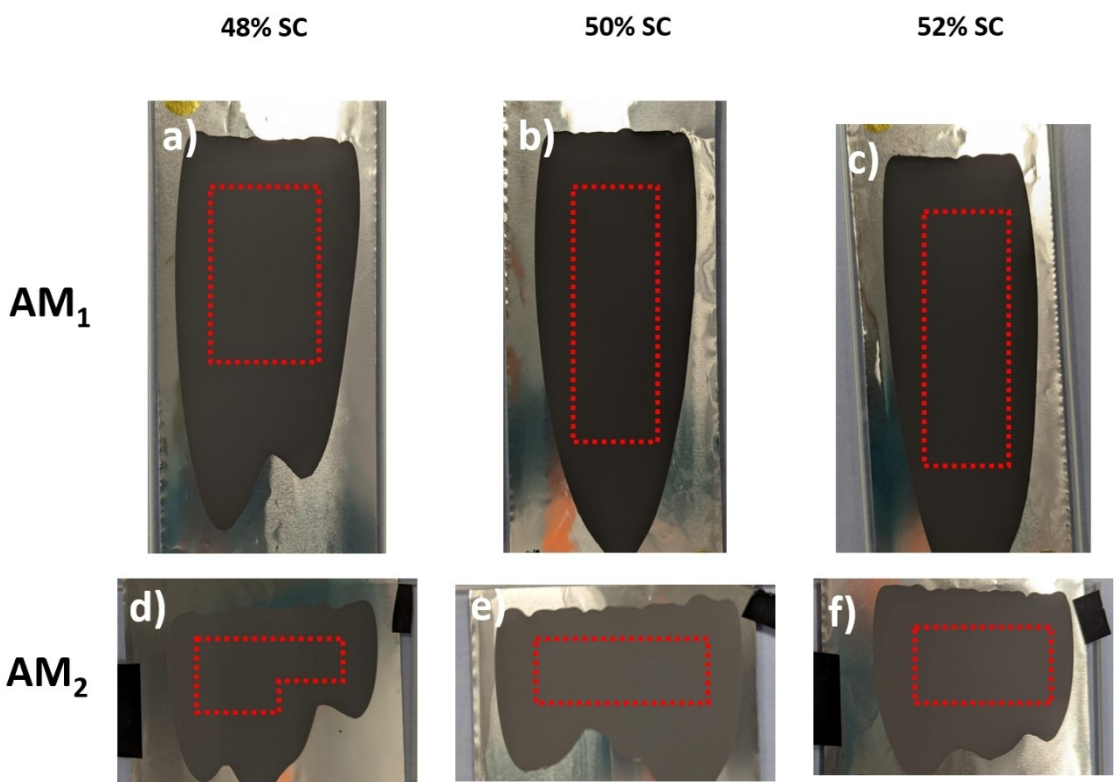


Figure 1. Casted SSB composite electrodes of AM₁, consisting of a) 48 % SC, b) 50 % SC and c) 52 % SC, of AM₂, consisting of d) 48 % SC, e) 50 % SC and f) 52 % SC. Punches were made only within the area specified in red.

The porosity was determined by calculating the difference between the actual and theoretical density of the electrode. The actual density was obtained by dividing the electrode's mass by its volume. The theoretical density, which assumes no void space, was derived from the individual densities of the electrode components (NMC811, SE, carbon and binder). Porosity was then calculated as the difference between 1 and the ratio of the actual density to the theoretical density.

Viscosity Measurements

The viscosity of the slurries was determined by a rheometer using a logarithmic sweep to apply a shear rate between 10 s⁻¹–1000 s⁻¹. The rheometer with parallel plate geometry was set to a 300 μm gap, 20°C and 2 min of soaking time before each measurement.

Cell Assembly and Effective Transport Characterization

Several round punches of 14 mm in diameter were taken from the dried electrodes and their thickness was measured. The electrodes were then pressed using a hydraulic press at 1.6 tons for 30 s. The press was released, and the electrodes were punched again to 10 mm diameter. This ensures that the inner electrodes are not damaged during preparation. The electrodes were then sandwiched between two Ni foils in an ionically blocking configuration and then inserted into a PEEK lined airtight press cell with stainless steel stamps. The stamps are then connected to the potentiostat to have a two electrode setup for EIS and direct current (DC) polarization measurements. The press cell was fastened after pressing to 1 ton to perform the EIS and DC polarization measurements.

Simulations

The CGMD Method

A Coarse-Grained Molecular Dynamics (CGMD) framework was developed and implemented in LAMMPS simulation software^[32] to model the behavior of the slurry and the electrode systems, relying on interactions among individual particles represented as beads, utilizing fitted FFs (Table S1). These interactions account for the materials involved in the slurry-based manufacturing process of the SSB cathode electrodes. The carbon-binder domain (CBD) represents a geometrical domain within the model, encapsulating carbon additives, binder and solvent in the case of the slurry, and only carbon and binder in the case of dry and calendered microstructures. The density (ρ_{CBD}) of the CBD constitutes an effective parameter utilized for further model optimization and Force Field (FF) parameterization. The FF utilized are the Lennard-Jones (LJ) and Gaussian-Hertzian (GH) which are available in the LAMMPS software^[32] and employed to model the entire manufacturing process.

The interactions among these particles are governed by the FFs that are parameterized to align with experimental observables. These encompassed the experimental viscosity in case of the slurry phase and the porosity and density of the dry and calendered electrodes. The calibration of the FF parameters consisted of a comparison between the simulation outputs and the experimental data along each manufacturing step. The parametrization started from already published work^[14,26] and moved up to reach our own parameterization according to the experimental data obtained in the present work. More details on the CGMD and FFs utilized in the simulation workflow are presented in the SI.

Simulation Workflow

The simulation entails solving Newton's equations of motion to generate a 3D microstructure of the SSB composite electrode under periodic boundary conditions (PBCs). All three dimensions remain periodic during the simulation of each phase, except for the calendering process, where only the x and y dimensions are periodic due to the application of pressure perpendicular to the z-axis. These conditions are applied to each manufacturing step (slurry, drying, and calendering), with the output of the preceding phase serving as input for the subsequent one, as illustrated in Figure 2.

This approach necessitates two sets of parameters: the first set is the manufacturing inputs, which determine the influence of each manufacturing process on the microstructure of the slurry and the dried and calendered electrodes, and the second set is the FF parameters, which govern the potential governing particles' interactions.

The simulation workflow of the slurry, drying, and calendering processes typically takes approximately 36, 48, and 24 hours, respectively, using one node with 360 GB of RAM and 1 processor (Intel® Xeon® CPU E5-2680 v4 @ 2.40 GHz, 40 cores) of the MatriCS platform (Université de Picardie Jules Verne).^[33]

Manufacturing Inputs

The electrode slurry composition and the two PSDs of the AM (AM_1 and AM_2) and SE (1 μm) are used as manufacturing inputs in the simulations. Throughout the simulation process, all manufacturing inputs were maintained as experimentally defined without further alterations.

The electrode composition comprises the weight percentages of the AM, SE, carbon additives, and binder along with the solvent content that was incorporated during the electrode fabrication. Therefore, the simulation involves a formulation for the dry composite consisting of 64% NMC, 30% LPSCl, and 6% CBD,

incorporating a total of 5051 particles. The number of particles was calculated based on the dry electrode mass of $0.139 \times 10^{-7} \text{ g}$ and the sizes of the AMs and SE were retrieved from the experimental PSDs and dry CBD size of 2.6 μm . Thus, the diameter of CBD particles varied depending on the simulation stage, where the CBD size (encapsulating carbon, binder and solvent) ranged from 6.9 to 8.0 μm depending on the SC of the slurry and 2.6 μm for the dried and the calendered electrodes. The CBD phase is discretized to a certain diameter size to ensure a good compromise between accuracy and computational efficiency

Initial Particle Localization

To initialize the simulations, the particles representing AM, SE and CBD are placed within a simulation box demonstrated in Figure S4. To prevent particle overlap, particles are stochastically distributed within a large simulation box measuring 716 $\mu\text{m} \times 716 \mu\text{m} \times 1000 \mu\text{m}$ based on an algorithm implemented in LAMMPS that prevents creating new particles closer than a certain distance to the previously created particles with respect to the simulation box size.

To ensure the proper initial generation of particles and the equilibration of the slurry, the temperature is set to 300 K and the pressure ramps from 0 to 1 bar. For drying and calendering, the CGMD simulation is in an isothermal-isobaric condition of 300 K and 1 bar, where the initial velocities of the particles are assigned randomly, adhering to a distribution corresponding to a temperature of 300 K. This is known as the NPT ensemble, where particles, pressure, and temperature remain constant which is a condition maintained throughout the slurry and drying simulations.

Viscosity

The workflow starts with simulating the slurry phase, allowing for the calibration of the simulated microstructures by comparing the simulated viscosities to the experimental values. To compute the viscosity of the simulated slurry model, a series of CGMD

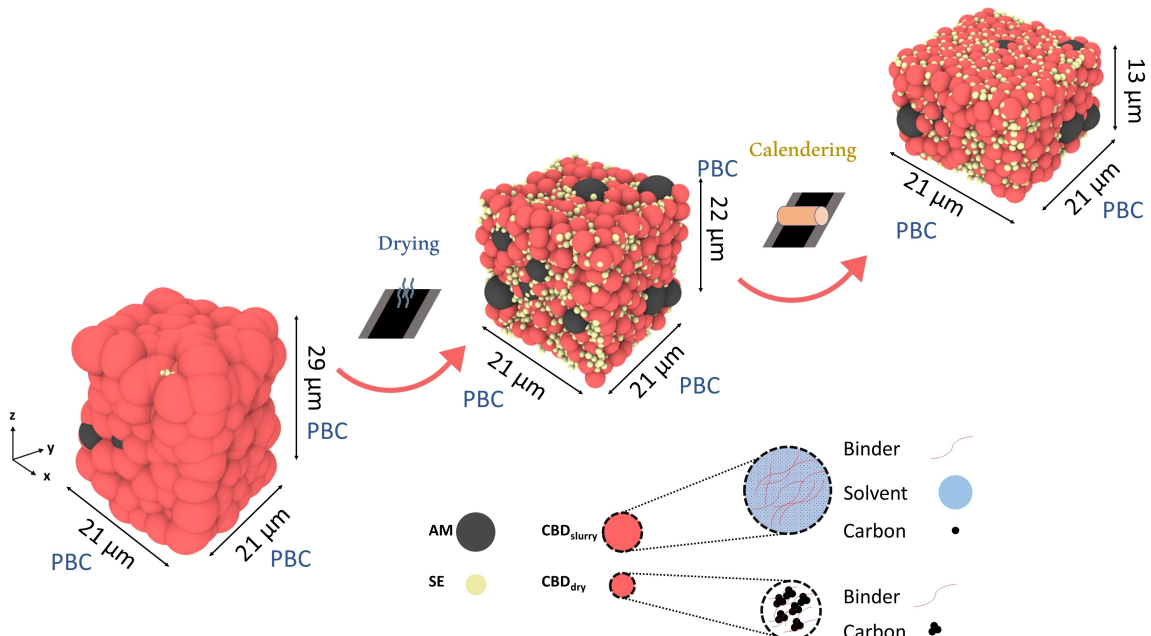


Figure 2. Schematic representation of the SSB composite cathode modeling workflow for the slurry-based manufacturing process. It consists of three main manufacturing models: slurry preparation, drying, and calendering. The black particles stand for the AM, the yellow particles for the SE and the red particles for the CBD.

simulations is conducted in a non-equilibrium state, assessing multiple viscosity values against applied shear rates.

To achieve this, the simulation box undergoes deformation in one lateral direction by adjusting the angle of the x-y plane relative to the x direction. The deformation rate equals the selected shear rate multiplied by the length of the simulation box in the y direction. Additionally, sufficient time is allocated for the simulation to converge towards its viscosity value. In this model, we utilized 7×10^7 timesteps, each of size $\Delta t = 0.001 \mu\text{s}$ as smaller Δt was tested and led to same results. The viscosity was derived by averaging the instantaneous viscosity values after the simulation convergence. Each simulation required approximately two days utilizing the computational hardware described above.

Effective Electronic and Ionic Conductivities

The electrode's effective electronic conductivity (σ_e) and effective ionic conductivity (σ_{ion}) serve as chosen parameters to provide quantitative assessments of the electrode's electronic and ionic percolation properties. These parameters are observables devised to encompass electronic and ionic properties of the simulated dried and calendered electrodes. Herein, the description of the voxel-based flux simulations to determine effective σ_e and σ_{ion} . The flux simulations were performed using the ConductoDict module of GeoDict (Math2Market).^[34] The microstructures resulting from the CGMD simulations were voxelized to be imported in GeoDict using an *in house* MATLAB script with a voxel size of $0.2 \mu\text{m}$.

The σ_e of the microstructures was determined by solving the Poisson equation within the simulation domain, while applying a 1 V potential difference between opposite sides along the z-direction (perpendicular to the calendering plane). Subsequently, Ohm's law was employed to derive the σ_e . Specifically, the intrinsic electronic conductivity values of AM and CBD phases were retrieved from the literature^[35–37] set to 0.005 Sm^{-1} and 15.93 Sm^{-1} ^[36–37] respectively, and the SE's intrinsic electronic conductivity was set to 0.0 Sm^{-1} as nonconductive phase. PBCs were considered for the outer xz and yz planes.

The σ_{ion} values are determined using the equation $\sigma_{ion} = \sigma_{bulk} \times (D_{ion}/D_{bulk})$, where σ_{bulk} represents the bulk conductivity of the SE of 1.25 mS cm^{-1} (provided by the supplier) and D_{ion} and D_{bulk} are the

effective and bulk diffusion coefficient for Li^+ within the SE conductive media. The D_{ion}/D_{bulk} ratio is calculated by solving Fick's first law within the SE domain, considering a concentration difference Δc between the outer xy planes. D_{ion} is obtained from the overall diffusive flux (j) using the equation: $D_{ion} = -j \times \text{length} / \Delta c$, then. Periodic boundary conditions are applied in lateral dimensions.

2. Results and Discussion

2.1. Slurry

The rheological properties of the slurry have significant influence on the electrode manufacturing process.^[38–40] We have measured the viscosity of our slurries due to their immense impact on final electrode characteristics. Therefore, viscosity was used as a metric for the quality and homogeneity of the coating. Since the solvent has high evaporation rates, the consistency of the viscosity would reflect the effect of the delay between pouring the slurry and the start of the coating process. Longer soaking times result in dense inhomogeneous slurry as the solvent evaporates and AM particles sink to the bottom (Figure 3). This results in an inconsistent heterogenous coat since SC would vary due to the evaporation rate of the solvent.^[41] Our objective was to ensure that all the coating procedures resulted in the same viscosity as a function of SC and shear rate using the same constant comma gap and coating speed.

In the context of slurry coating, slurry viscosity serves as a valuable metric for the state of the slurry and elucidates the structural alterations occurring within the slurry under applied shear stress. By analyzing the viscosity behavior, we can garner insights into the evolution of the slurry's internal structure throughout the coating process. In Figure 4, four samples were used to obtain each experimental viscosity-shear rate curve.

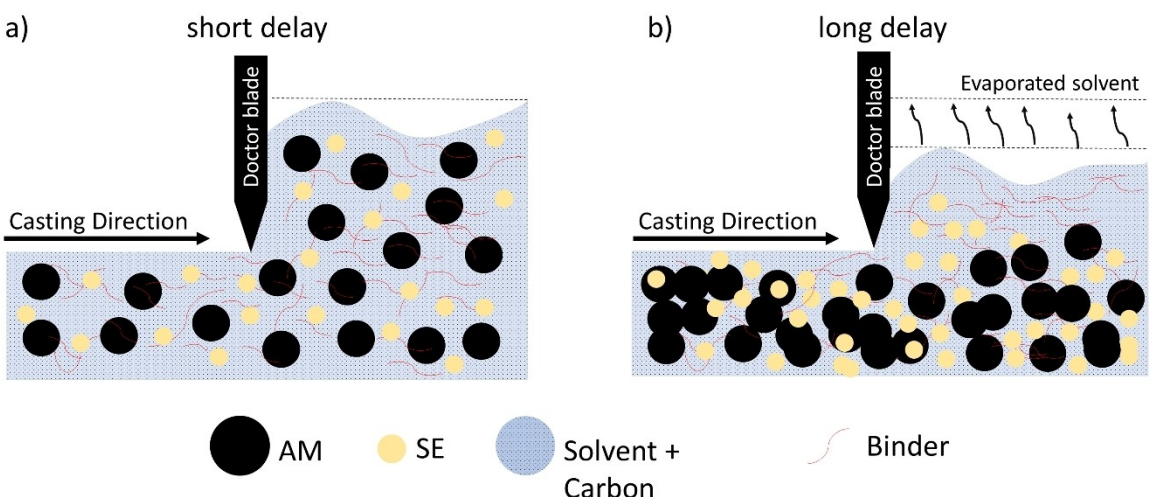


Figure 3. Schematic representation of the soaking time effect on the components of the SSB slurry.

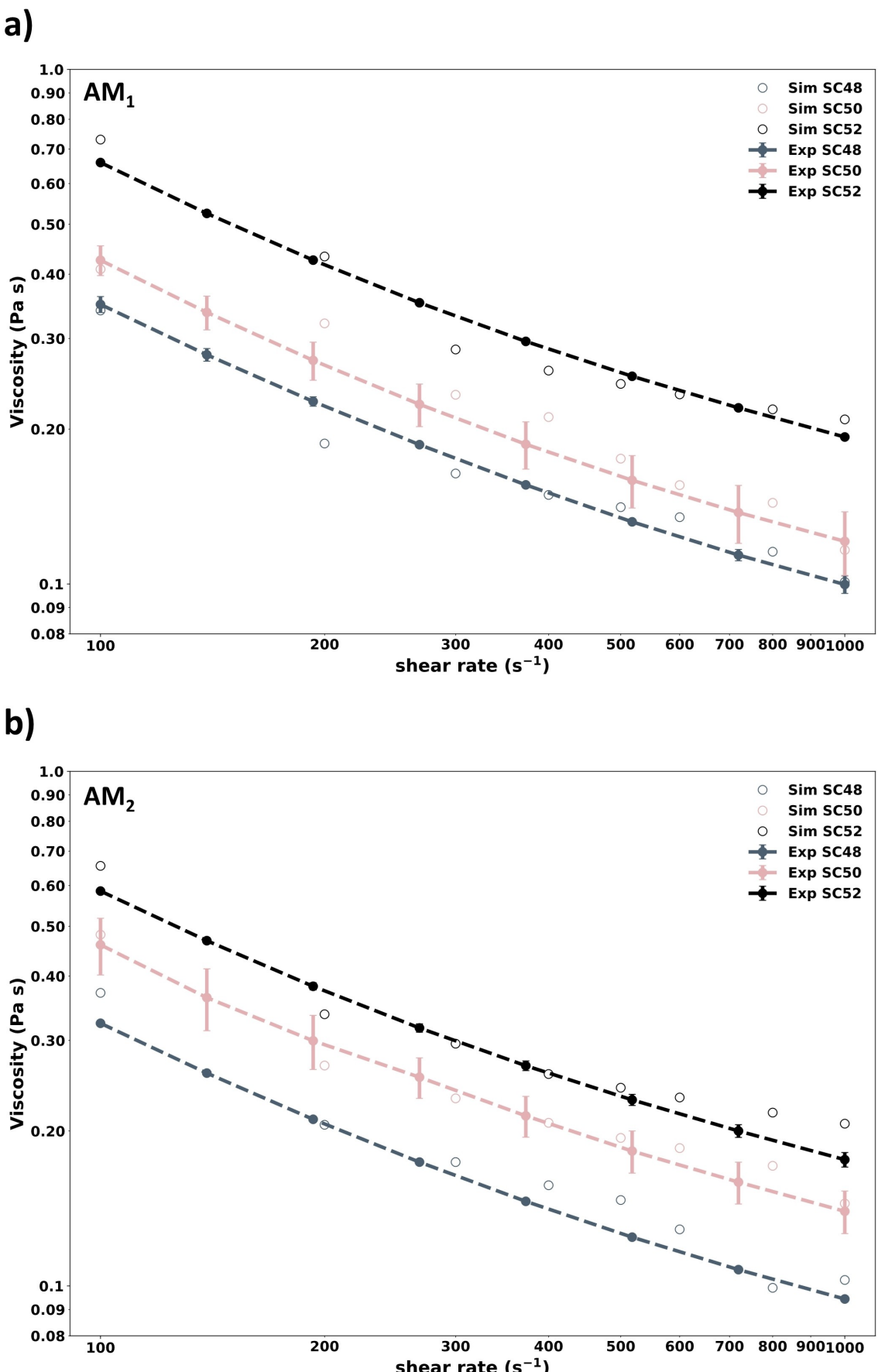


Figure 4. Viscosity-shear rate curves obtained experimentally compared to the simulated results obtained via non-equilibrium CGMD.

The simulated viscosity values of both AM_1 and AM_2 microstructures fluctuate around the experimental values. Viscosity shows a direct correlation with the SC where a slight increase in the SC of (4%) can cause the viscosity values to be more than 2-fold higher as a function of shear rate. The desired viscosity range is between 0.3 and 0.6 Pa·s to enable uniform electrode casting. Experimentally, our goal was to ensure a minimal human error's influence on viscosity consistency under the shear stress applied by the doctor blade during casting.

The results obtained from the non-equilibrium CGMD viscosity simulations were fitted to the experimental observations. This high agreement between the simulated and experimental values of viscosity, in the shear rate frequency range investigated, indicates that the slurry model is well-suited to function as a digital representation or computational tool provided the right FF parameters are selected, facilitating further assumptions and predictions for subsequent process steps.

The fitting of the experimental viscosity values was performed manually incrementally, by adjusting one FF parameter per simulation until a viscosity value nearby the error margins of the experimental viscosity was achieved for a given shear rate. Once this was accomplished, the simulations for entire viscosity curve were performed to ensure that the entire curve was derived from the same combination of FF parameters. It is evident from Figure 4 that the viscosity is in direct correlation with the SC: as the SC increases the viscosity increases as well. The simulated viscosity values depend on the particle-size based LJ and GH FFs of the model. The LJ parameters are used to describe the repulsion-attraction interparticle forces, tuning mainly the average distance between two distinct particles. The GH forces affect only the normal and tangential forces between two particles only when they overlap. As the diameter of the CBD decreases in slurry microstructures with higher SC, there is a higher potential for the SE and AM particles to overlap which introduces more forces and thereby higher viscosity. However, there is no significant difference between the viscosity values of AM_1 and AM_2 which could be attributed to the low wt.% in the slurry composition.

2.2. Drying and Calendering

During the drying stage, we implement a homogeneous solvent evaporation model,^[29] which posits that all CBD particles containing solvent will instantly contract to their solid-state size of 2.6 μ m. The resulting microstructures differ only in terms of PSDs of AM_1 and AM_2 , as well as the initial position resulting from the previous slurry simulation step in the workflow. When the microstructures have the same AM PSD, the only difference is the particle arrangement induced by the size of the CBD particles during the slurry stage. Following this contraction, the system can equilibrate. To simulate the phase transition from slurry to a dried electrode, we adjust the FF parameters by enhancing the attractive and elastic interactions. This adjustment reflects the stronger particle bonds formed by binder

bridges and the mechanical integrity of the dried electrode. As a result, the electrode thickness decreases from top to bottom. Throughout the simulation, the PBCs are maintained in all dimensions and the temperature is maintained at 300 K within the NPT ensemble.

Electrode calendering is critical for improving its conductivity and mechanical strength, which are crucial for maximizing the volumetric energy and power densities of battery cells. For SSB cells, the goal is to create highly compact electrodes with minimal porosity, enhancing ionic conductivity, rate capabilities, and the utilization of AM.^[16,42] Therefore, understanding the impact of calendering on the electrode microstructure is essential for identifying optimal compression parameters that address these challenges. Our calendering model simulates the actual calendering process by using a plane moving downward at a constant speed to compress the electrode. The interactions between the wall and the particles are modeled using GH FFs, with force parameters detailed in Table S1 in the SI. We assume that the CBD phase is 50% composed of nanopores, and this nanoporosity decreases during calendering.^[43,44] During calendering, the PBCs are applied in the lateral x and y directions, while the surface perpendicular to the z-axis remains fixed. As the plane descends, the particles rearrange due to the force imposed on them.

Figure 5 depicts the experimental and simulated density and porosity values for microstructures composed of AM_1 and AM_2 coming from slurries with 48%, 50% and 52% SC. The experimental density and porosity values are obtained from two different punches of the same dried electrode. The only obvious trend is that the density of the cathodes after drying directly correlates with the SC of the slurry. However, the microstructures do not continue this trend after calendering. Since the drying procedure removes the solvent after the slurry formulation, the porosity and density values may not show a monotonic correlation with the SC. Nevertheless, to come up with a concrete conclusion a high number of samples is needed to statistically validate this outcome. The simulation outcomes are compared with experimental density and porosity data, in Figure 5a and 5c, where both AMs (AM_1 and AM_2) result in a dry electrode density between 1.0–1.5 g/cm³ and a calendered electrode density between 2.0–2.5 g/cm³ with AM_2 dry density being slightly higher. However, the AM_1 microstructures have higher calendered density. This becomes evident from their porosity data in Figure 5b and d, where the smaller particles of AM_1 results in higher dry porosity (approx. 70% for 48% and 50% SC and 50% for 52% SC) and both AMs have a calendered porosity between 20%–30%.

As all CBD particles of the simulated microstructures have the same size after drying, the PSDs of the AM and the particles arrangement in the microstructures are the main differences in the resulting simulated microstructures. However, the simulated microstructures show good agreement with the experimental results by capturing the structural properties in terms of density and porosity. This means that SSB electrode microstructures cannot be fully optimized by only focusing on the drying process and the initial properties of the microstructural components play a significant role. AM_1 has lower densities for

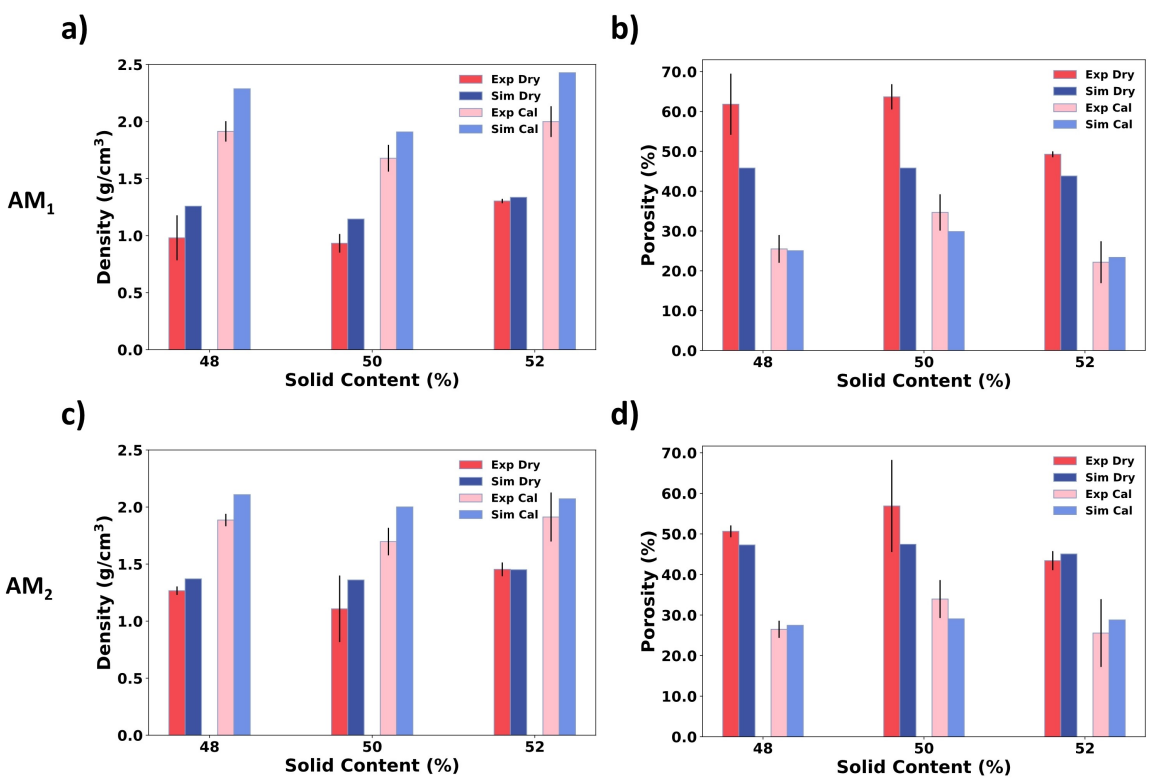


Figure 5. Comparison between simulated and experimental values for different SC of a) density and b) porosity of the dried and calendared AM₁ and c) density and d) porosity of the dried and calendered AM₂.

the dried electrodes but can be higher after calendering when compared to AM₂ which may be attributed to the different interactions happening during drying and calendering. This becomes more evident when observing that the smaller AM₁ particles yield a higher porosity after drying but compact more when calendered resulting in higher densities.

Generally, pores are undesired in SSB electrodes because they form a non-conductive medium that interrupts the electronic and ionic percolation networks. Achieving very low porosity values requires the exclusion of binder, as its elastic properties cause the electrodes to recover part of the lost thickness after calendering. While it might seem that applying higher pressure could solve this issue, such an approach is ultimately destructive to the electrodes.^[45]

2.3. Simulated Microstructures

The simulation results elucidate the evolution of the microstructures of AMs (AM₁ and AM₂) at various stages of the solid-state battery electrode manufacturing process, specifically during slurry preparation, drying, and calendering, as depicted in Figure 6. Initially, in the slurry stage, the AM and SE are predominantly covered with CBD. These CBD particles exhibit substantial overlap, effectively representing the continuum nature of the solvent matrix. During the drying stage, as the solvent evaporates, the microstructure undergoes significant changes. The CBD particles, originally dispersed within the

solvent, shrink to a size of approximately 2.6 μm. This shrinkage represents solvent loss and densification of the microstructure, leading to a more compact arrangement of the particles. In the final calendering stage, the dried microstructures are compressed to achieve the desired density and surface smoothness. This pressing aligns and compacts the particles to mimic the calendered state. The simulations provide insights into the morphological transformations that occur at each stage, highlighting the critical role of the CBD particle behavior and solvent dynamics in determining the final microstructural properties of the solid-state battery electrodes.

2.4. Effective Electronic and Ionic Conductivities

Figure 7 presents the experimental impedance data of the electrodes prepared with AM₁ and AM₂ PSDs derived from different SC slurries (48%, 50%, and 52%) in an ionic blocking symmetric cell setup. The corresponding transmission line model (TLM) impedance presented in Equation 1 enables the extraction of the effective electronic transport properties of the composites. The total cell impedance Z of the ionic blocking cell is influenced by the impedance of the electron-conducting phase z_e , the ion-conducting phase z_{ion} and the interface impedance between these two phases z_{int} . L represents the thickness of the slurry-based electrode.^[46]

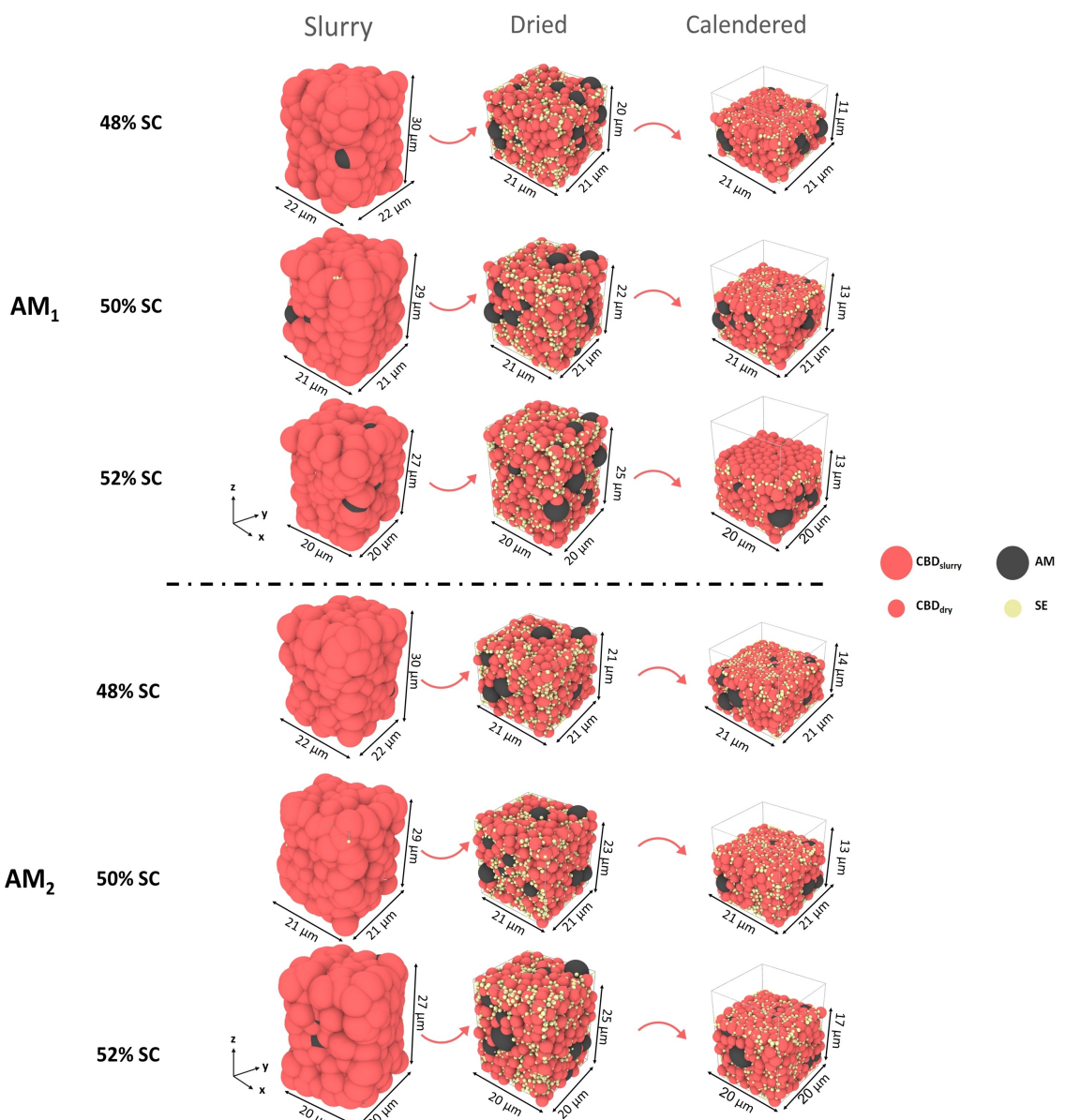


Figure 6. Resultant microstructures for 48%, 50% and 52% SC of AM_1 and AM_2 from the slurry-based manufacturing Simulations of the SSB composite cathode. It consists of three main manufacturing stages: slurry, drying, and calendering. The black particles stand for the AM, the yellow particles for the SE and the red particles for the CBD.

$$Z = \frac{z_{\text{ion}} z_e}{z_{\text{ion}} + z_e} L + \frac{2 z_e^2 \sqrt{z_{\text{int}}}}{(z_{\text{ion}} + z_e)^2} \cdot \frac{\cosh(L \sqrt{\frac{z_{\text{ion}} + z_e}{z_{\text{int}}}}) - 1}{\sinh(L \sqrt{\frac{z_{\text{ion}} + z_e}{z_{\text{int}}}})} \quad (1)$$

The electronic impedance z_e is determined by the bulk resistance of the materials forming the composite r_e and the interfacial impedance z_{int} at the phase boundaries between the AM particles and the CBD. This interfacial impedance arises from electronic charge transfer across the AM-CBD interface and is modeled by a parallel constant phase element cpe_{di} . The ionic impedance z_{ion} is characterized by an ohmic resistance r_{ion} . In this system, non-faradaic behavior is assumed since there is no charge transfer between the ion-conducting and electron-

conducting phases in the symmetric cell.^[9] A comparison between the electronic resistance values obtained from impedance analysis and those determined through DC polarization measurements (Figure S2, SI) confirms the validity of both methodologies detailed in Table S3.

$$\sigma_e = \frac{L}{Z \times A} \quad (2)$$

Experimental σ_e values are calculated by Equation 2 where A is the electrode punch area. Our approach of using σ_e of the electronic conducting media as a general indication of electrode quality is particularly useful. Our results provide a quantitative means to evaluate manufacturing conditions. We

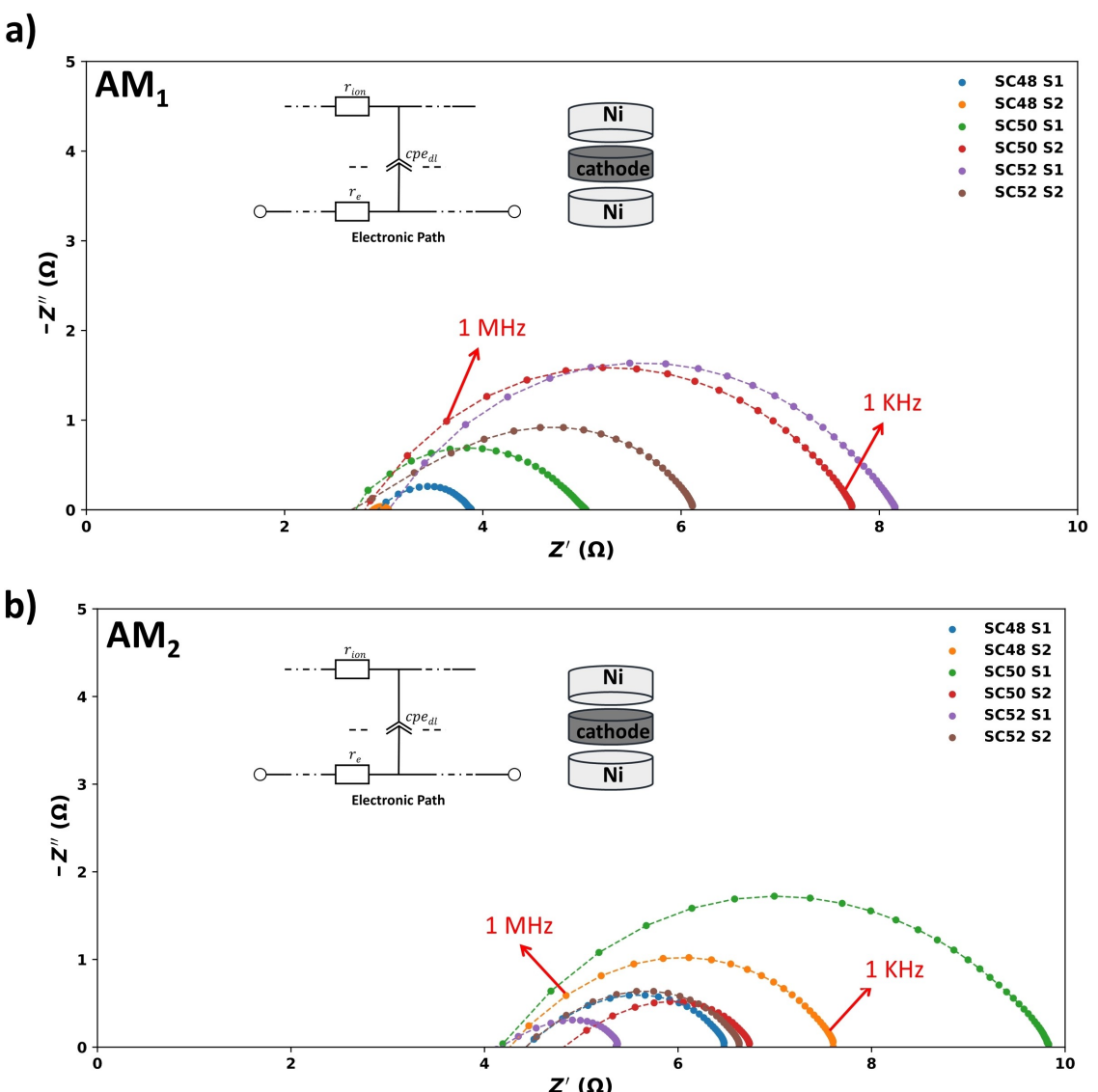


Figure 7. Nyquist plots of impedance data of the a) AM₁ and b) AM₂ with varying SC are depicted alongside the TLM. The impedance spectra were measured in ionic blocking symmetric cells with an electronic connection, facilitating the evaluation of effective electronic transport properties.

observe in Figure 8a that there is a difference (depending on the SC) within the experimental σ_e values of the thin AM₁ and thick AM₂ with AM₂ having almost double the electrode thickness. Both have opposite trends vs. SC, where AM₁ shows a decreasing trend and AM₂ an increasing one. Since the main difference between the experimental electrodes is the electrode thickness. This thickness difference may cause interruptions in the electronically conductive phase of the CBD.

A previously reported study^[47] on interlaboratory reproducibility highlights the challenges of comparing absolute conductivity values due to significant variability, even when identical samples are tested across multiple labs. This variation, attributed to factors like electrode microstructure and particle arrangement, resulted in total conductivity ranges of up to $4.5 \text{ mS} \cdot \text{cm}^{-1}$, with a relative standard deviation of 35% to 50%. Given the complexity of the SSB electrode microstructures, such variability is expected, particularly due to the sensitivity of

conductivity to the precise particle locations, which are difficult to control using classical wet processing. In our study, experiments were conducted using high-quality, standardized equipment at Umicore, where our electrodes demonstrated homogeneity through visual inspection and SEM analysis, though SEM data remain confidential. Therefore, for our study's primary goal of validating our modeling approach through experimental comparison, the number of samples used is sufficient to provide meaningful insights.

However, the simulated AM₁ and AM₂ microstructures show a decreasing trend of σ_e vs. SC with AM₁ having slightly higher σ_e values. The simulated microstructures show that due to processing effects, there is a 93.5% reduction in the intrinsic electronic conductivity of the conductive phases within the electrode mainly the CBD. Nevertheless, σ_e should not be the limiting factor in the cathode rate capabilities since the ionic conductivity is usually lower than the electronic.^[3] Figure 8b

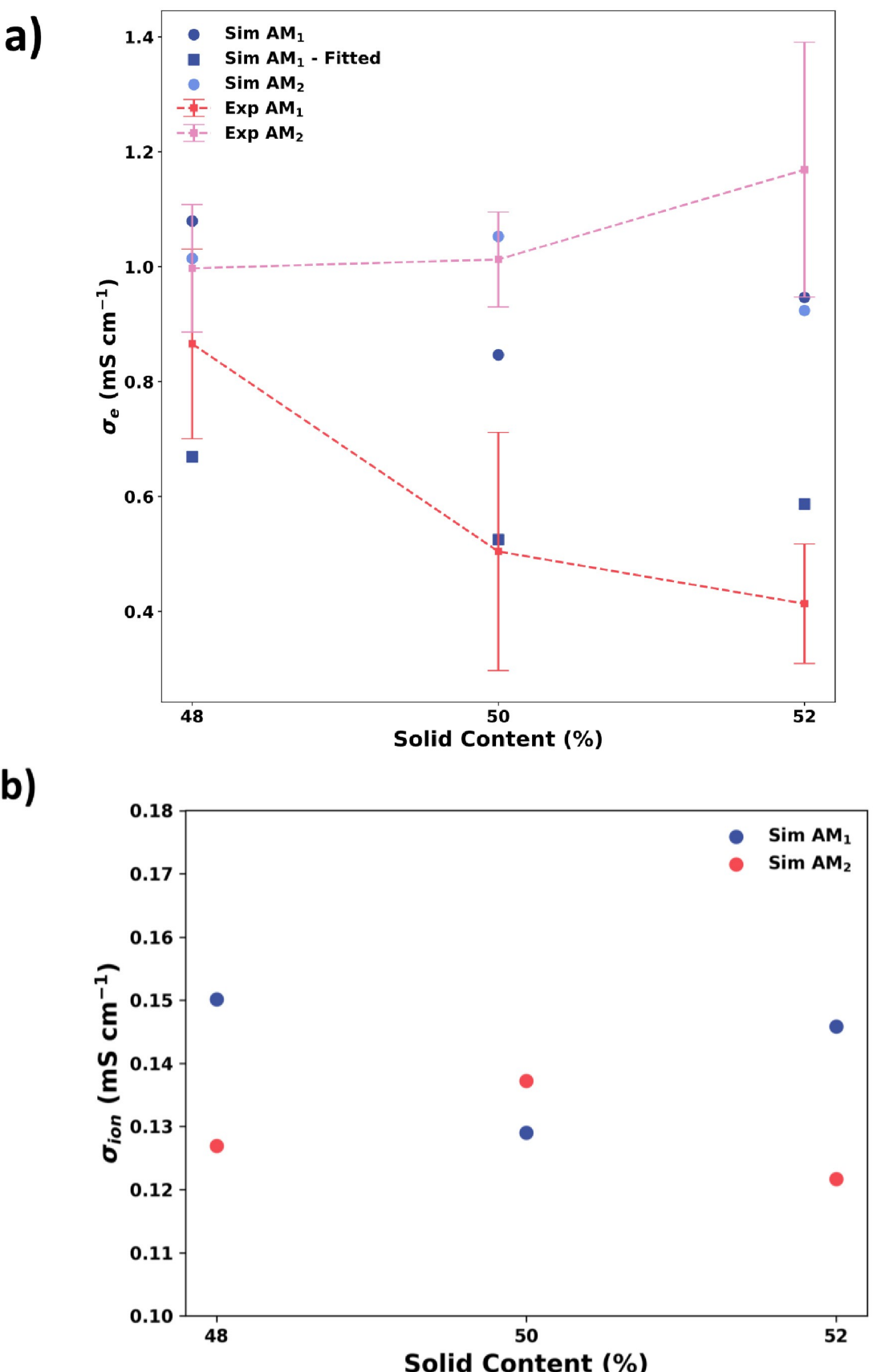


Figure 8. a) Electrode's simulated and experimental σ_e as a function of SC for AM₁ and AM₂ slurry-based electrodes. In addition to the simulated AM₁ σ_e values when CBD electronic conductivity is fitted. b) Electrode's simulated σ_{ion} as a function of SC for AM₁ and AM₂ slurry-based electrodes.

shows the σ_{ion} for the calendered AM₁ and AM₂ simulated microstructures for different slurry SC where the microstructures show very close σ_{ion} values that range 12–15 mScm⁻¹. AM₁ simulated microstructures have higher σ_{ion} values for the case of 48% and 52% SC which is attributed to higher volume fraction of SE and contact with the AM particles.

To gain a deeper understanding of the differences in σ_e between the experimental microstructures depending on the SC and AM PSD, as we expect that CBD intrinsic conductivity would depend on SC values, we fitted the intrinsic conductivity of the CBD within the simulated microstructure AM₁ to be 9.88 Sm⁻¹, as shown in Figure 8a. This analysis reveals that the primary source of variation in σ_e values stems from the geometrical heterogeneities within the CBD phase of the two microstructures. As shown in the literature,^[12,16,48] different electrodes with the same composition and porosity differ in performance. This signifies that geometrical heterogeneities induced by the exact particle/pores arrangement significantly impact the conductivities and electrode's overall performance since they are directly correlated with interfacial contacts between the particles and/or between phases within the electrode. Figure 9a provides a comparison of the CBD phase, highlighting the distribution of CBD particles (red) and pores (black). It is evident from Figure 9a that the AM₁ microstructures, derived from 50% and 52% SC slurries, exhibit a higher prevalence of pores between the CBD particles. These pores contribute to the observed differences in electronic and ionic conductivities by disrupting the conductive pathways within the CBD phase. The difference in CBD conductivity values of the AM₁ microstructures can be attributed to variations in the distribution of conductive carbon and insulating binder within the slurry. The conductive carbon and binder not only influence the overall conductivity but also affect the mechanical and structural integrity of the microstructures. A heterogeneous distribution of these components leads to an uneven formation of conductive networks and increased pore formation, which in turn reduces the effective conductivity. Since porosity represents a nonconductive phase within SSB electrodes, its presence significantly contributes to the formation of tortuous ionic and electronic pathways resulting in higher electrode impedance. Consequently, calendering is employed to enhance both ionic and electronic conductivities in SSBs, with minimal porosity being a key target to achieve optimal performance. We compared the cross sections of dry and calendered microstructures from the simulations of the 48% solid content case, as shown in Figure 9b, with volume fraction graphs for all simulated electrodes provided in the SI (Figure S5a and b). Figure 9b shows that the CBD and SE particles have a higher interparticle contact in the case of AM₁ microstructures and higher volume fraction compared to the porosity in Figure S5a and b. This attributes to the higher electronic and ionic conductivity of AM₁ shown in Figure 8a and b. However, comparing and segmenting experimental electrode cross-sectional SEM images is challenging, as these images provide only 2D information, while our model is fully 3D resolved. Advanced techniques like FIB-SEM or computer tomography also face difficulties in accurately segmenting volume fractions of CBD

and SE due to minimal contrast differences. This issue, highlighted in a previous publication,^[49] remains a challenge with current characterization technologies. Moreover, the spatial arrangement and connectivity of the CBD particles play a crucial role in determining the σ_e . In the AM₁ microstructures with higher porosity, the conductive pathways are interrupted more frequently, resulting in lower overall conductivity. Conversely, a more homogeneous distribution of CBD particles and fewer pores would enhance the connectivity of the conductive network, thereby increasing σ_e . These findings underscore the importance of optimizing the formulation and processing parameters of the slurry to minimize geometric heterogeneities and enhance the conductivity of the CBD phase.

3. Conclusions

Solid-state batteries have shown significant promise for advancing energy storage technologies, especially for high-demand applications such as electric vehicles. This study has focused on understanding and optimizing the microstructures resulting from slurry-based manufacturing processes of SSB composite cathodes to enhance their performance. We present a 3D-resolved physics-based computational workflow able to simulate thoroughly the manufacturing process of SSB composite electrodes using NMC811 as AM. Electrodes' composition, PSDs of the AM and SE and slurries SCs are all used as manufacturing inputs for our workflow. Our study presents, as far as we know, the first-ever comparison of an innovative electrode manufacturing modeling framework with systematically acquired experimental data, marking a significant contribution to the field. While we acknowledge the importance of factors such as varying active material percentages, our current work was designed to focus on a limited set of variables to ensure a manageable scope and thorough analysis. Investigating the impact of changes in AM percentages would require a broader study, which is beyond the present work's scope. However, we recognize the potential value of this research direction and plan to explore it in future studies to further optimize the performance of composite cathodes in SSBs.

We are also interested in establishing a direct correlation between elastic properties such as Young's modulus and the FF parameters in our CGMD model but remains challenging with current methodologies. Presently, we utilized a top-down approach in our previous work^[29] by calibrating FF parameters to align our simulations with experimental data, such as fitting micro-indentation curves to match observed behaviors. While this method effectively ensures consistency with experimental results, it does not provide a direct linkage between mechanical properties and FF parameters due to the complexity and computational intensity involved. Acknowledging the importance of this relationship, we plan to pursue future research aimed at developing more sophisticated modeling techniques that can directly connect material properties like Young's modulus with our CGMD parameters. This advancement will enhance the accuracy and predictive capability of our simu-

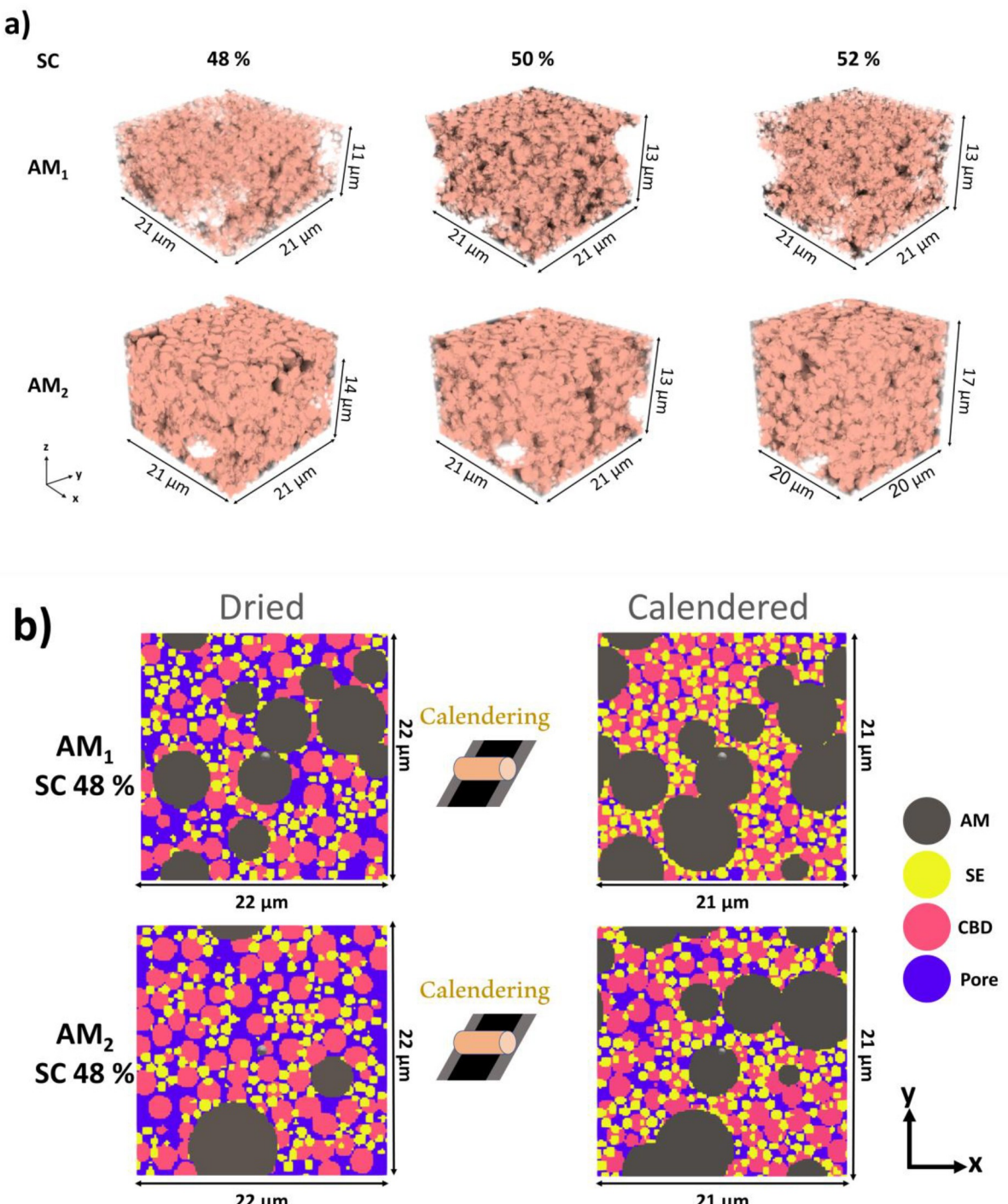


Figure 9. a) Representation of the CBD (pink) and pore (black) phases of the simulated AM₁ and AM₂ microstructures for 48%, 50% and 52% SC. b) images of the cross-sections of the simulated AM₁ and AM₂ microstructures of 48% SC.

lations, thereby improving the understanding and performance optimization of SSB composite cathodes.

The simulation results are in excellent agreement with experimental data in regards to the slurry viscosity, the dried and the calendered electrode density, porosity and σ_e . The well-fitted simulation results demonstrate that this workflow consisting of several sequentially coupled models is a good represen-

tation of the real wet manufacturing process to produce electrodes with similar features. Particularly, the same FF parameters are used to fit different SCs and PSDs of the AM. This highlights again the chemical neutrality of our approach. The rheological properties of the slurry play a crucial role in determining the quality and homogeneity of the electrode coating. We aimed to understand the relation of viscosity with

the uniformity of the produced electrodes. We find that variations in soaking times and SC significantly affect slurry homogeneity and, consequently, the final electrode microstructure.

Furthermore, the effective electronic conductivity of the electrode is utilized as a quantitative metric to study the electrode microstructure arising from slurries with varying SC. AM₁ and AM₂ microstructures exhibit different trends in effective electronic conductivity with varying SC, however, the overall effective electronic conductivity should not be the limiting factor for cathode power capabilities, given that ionic conductivity is typically lower.

This comprehensive modeling and experimental study underscores the complex interplay between slurry composition, microstructure design, and slurry based-manufacturing processes in determining the performance of SSB electrodes and cells. Our findings suggest that consistent slurry viscosity is crucial for uniform electrode coating and optimizing particle size and binder content is essential to decrease electrode porosity, resulting in improved ionic and electronic conductivities. An important future research direction involves simulating electrode drying rates to explore their impact on microstructural heterogeneities. Our group, as part of the ARTISTIC initiative, developed a physics-based model^[28] for LIBs capable of simulating the drying process of NMC-based slurries, with a specific focus on CBD migration. This model effectively captures the transition from a liquid-like slurry to a solid electrode. Through simulating several different drying rates, it was found that higher drying rates lead to increased CBD concentration and migration within specific regions and time frames.

Acknowledgements

M.A. acknowledges Ben Meynaerts from Umicore for the technical support provided in the lab. M.A., V.S. and A.A.F. acknowledge Ben Meynaerts, Anna-Katharina Hatz, Duancheng Ma, Anh Ha Dao, and Laura Albero Blanquer from Umicore for all technical discussions and feedback within the aspect of this study. M.A., V.S. and A.A.F. acknowledge the support by Umicore within the DESTINY PhD Programme, which has received funding from European Union's Horizon2020 research and innovation programme under the Marie Skłodowska-Curie Actions COFUND (Grant Agreement #945357). A.A.F. acknowledges the European Union's Horizon 2020 research and innovation program for the funding support through the European Research Council (grant agreement 772873, "ARTISTIC" project). A.A.F. and F.M.Z. acknowledge the European Union's Horizon Europe research and innovation programme under grant agreement No. 101069686 (PULSELiON). A.A.F. acknowledges Institut Universitaire de France for the support.

Conflict of Interests

The authors declare no conflict of interest.

Data Availability Statement

The data that support the findings of this study are available from the corresponding author upon reasonable request.

- [1] J. Janek, W. G. Zeier, *Nat. Energy* **2016**, *1*(9), 1.
- [2] J. Janek, W. G. Zeier, *Nat. Energy* **2023**, *8*, 230.
- [3] D. Bistri, A. Afshar, C. V. Di Leo, *Meccanica* **2021**, *56*, 1523.
- [4] M. Balaish, J. C. Gonzalez-Rosillo, K. J. Kim, Y. Zhu, Z. D. Hood, J. L. M. Rupp, *Nat. Energy* **2021**, *6*(3), 227.
- [5] P. Adeli, J. D. Bazak, K. H. Park, I. Kochetkov, A. Huq, G. R. Goward, L. F. Nazar, *Angew. Chem. Int. Ed.* **2019**, *58*, 8681.
- [6] C. Yu, F. Zhao, J. Luo, L. Zhang, X. Sun, *Nano Energy* **2021**, *83*, 105858.
- [7] A. Bielefeld, D. A. Weber, J. Janek, *ACS Appl. Mater. Interfaces* **2020**, *12*, 12821.
- [8] Y. G. Lee, S. Fujiki, C. Jung, N. Suzuki, N. Yashiro, R. Omoda, D. S. Ko, T. Shiratsuchi, T. Sugimoto, S. Ryu, J. H. Ku, T. Watanabe, Y. Park, Y. Aihara, D. Im, I. T. Han, *Nat. Energy* **2020**, *5*, 299.
- [9] P. Minnmann, L. Quillman, S. Burkhardt, F. H. Richter, J. Janek, *J. Electrochim. Soc.* **2021**, *168*, 040537.
- [10] P. Minnmann, J. Schubert, S. Kremer, R. Rekers, S. Burkhardt, R. Ruess, A. Bielefeld, F. H. Richter, J. Janek, *J. Electrochim. Soc.* **2024**, *171*, 060514.
- [11] G. Deysher, P. Ridley, S. Y. Ham, J. M. Doux, Y. T. Chen, E. A. Wu, D. H. S. Tan, A. Cronk, J. Jang, Y. S. Meng, *Materials Today Physics* **2022**, *24*, 100679.
- [12] M. Alabdali, F. M. Zanotto, M. Chouchane, A. C. Ngandjong, V. Viallet, V. Seznec, Y. S. Meng, A. A. Franco, *Energy Storage Mater.* **2024**, 103527.
- [13] M. Alabdali, F. M. Zanotto, V. Viallet, V. Seznec, A. A. Franco, *Curr. Opin. Electrochim.* **2022**, 36.
- [14] M. Alabdali, F. M. Zanotto, M. Duquesnoy, A.-K. Hatz, D. Ma, J. Auvergniot, V. Viallet, V. Seznec, A. A. Franco, *J. Power Sources* **2023**, *580*, 233427.
- [15] A. Bielefeld, *Batteries & Supercaps* **2023**, 6.
- [16] A. Bielefeld, D. A. Weber, R. Rueß, V. Glavas, J. Janek, *J. Electrochim. Soc.* **2022**, *169*, 020539.
- [17] F. Duffner, N. Kronemeyer, J. Tübke, J. Leker, M. Winter, R. Schmuck, *Nat. Energy* **2021**, *6*(2), 123.
- [18] D. H. S. Tan, Y. S. Meng, J. Jang, *Joule* **2022**, *6*, 1755.
- [19] J. Schnell, T. Günther, T. Knoche, C. Vieider, L. Köhler, A. Just, M. Keller, S. Passerini, G. Reinhart, *J. Power Sources* **2018**, *382*, 160.
- [20] T. Ates, M. Keller, J. Kulisch, T. Adermann, S. Passerini, *Energy Storage Mater.* **2019**, *17*, 204.
- [21] Y. J. Nam, D. Y. Oh, S. H. Jung, Y. S. Jung, *J. Power Sources* **2018**, *375*, 93.
- [22] J. Zhang, H. Zhong, C. Zheng, Y. Xia, C. Liang, H. Huang, Y. Gan, X. Tao, W. Zhang, *J. Power Sources* **2018**, *391*, 73.
- [23] C. Singer, S. Schmalzbauer, R. Daub, *J. Energy Storage* **2023**, *68*, 107703.
- [24] A. C. Ngandjong, A. Rucci, M. Maiza, G. Shukla, J. Vazquez-Arenas, A. A. Franco, *J. Phys. Chem. Lett.* **2017**, *8*, 5966.
- [25] A. A. Franco, A. Rucci, D. Brandell, C. Frayret, M. Gaberscek, P. Jankowski, P. Johansson, *Chem. Rev.* **2019**, *119*, 4569.
- [26] T. Lombardo, J. B. Hoock, E. N. Primo, A. C. Ngandjong, M. Duquesnoy, A. A. Franco, *Batteries & Supercaps* **2020**, *3*, 721.
- [27] A. Rucci, A. C. Ngandjong, E. N. Primo, M. Maiza, A. A. Franco, *Electrochim. Acta* **2019**, *312*, 168.
- [28] T. Lombardo, A. C. Ngandjong, A. Belhcen, A. A. Franco, *Energy Storage Mater.* **2021**, *43*, 337.
- [29] A. C. Ngandjong, T. Lombardo, E. N. Primo, M. Chouchane, A. Shodiev, O. Arcelus, A. A. Franco, *J. Power Sources* **2021**, *485*, 229320.
- [30] M. Chouchane, A. Rucci, T. Lombardo, A. C. Ngandjong, A. A. Franco, *J. Power Sources* **2019**, *444*, 227285.
- [31] A. Shodiev, E. N. Primo, M. Chouchane, T. Lombardo, A. C. Ngandjong, A. Rucci, A. A. Franco, *J. Power Sources* **2020**, *454*, 227871.
- [32] LAMMPS Molecular Dynamics Simulator, <https://www.lammps.org/>, accessed: June, 2024.
- [33] Matrics Platform – Shared platform for the research laboratories of the University of Picardie Jules Verne, <https://www.matrics.u-picardie.fr/en/home/>, accessed: June, 2024.
- [34] GeoDict simulation software Release 2023, by Math2Market GmbH, Germany, <https://doi.org/10.30423/release.geodict2023>, accessed: June, 2024.
- [35] R. Amin, Y.-M. Chiang, *J. Electrochim. Soc.* **2016**, *163*, A1512.
- [36] C. Liu, T. Lombardo, J. Xu, A. C. Ngandjong, A. A. Franco, *Energy Storage Mater.* **2023**, *54*, 156.

- [37] B. L. Trembacki, A. N. Mistry, D. R. Noble, M. E. Ferraro, P. P. Mukherjee, S. A. Roberts, *J. Electrochem. Soc.* **2018**, *165*, E725.
- [38] K. B. Hatzell, M. B. Dixit, S. A. Berlinger, A. Z. Weber, *J. Mater. Chem. A* **2017**, *5*, 20527.
- [39] W. Bauer, D. Nötzzel, *Ceram. Int.* **2014**, *40*, 4591.
- [40] G. W. Lee, J. H. Ryu, W. Han, K. H. Ahn, S. M. Oh, *J. Power Sources* **2010**, *195*, 6049.
- [41] Y. Komoda, K. Ishibashi, K. Kuratani, K. Suzuki, N. Ohmura, H. Kobayashi, *J. Power Sources* **2023**, *568*, 232983.
- [42] S. Li, Y. Sun, N. Li, W. Tong, X. Sun, C. T. Black, S. Hwang, *Nano Lett.* **2022**, *22*, 4905.
- [43] L. Zielke, T. Hutzenlaub, D. R. Wheeler, C. W. Chao, I. Manke, A. Hilger, N. Paust, R. Zengerle, S. Thiele, *Adv. Energy Mater.* **2015**, *5*, 1401612.
- [44] J. Xu, A. C. Ngandjong, C. Liu, F. M. Zanotto, O. Arcelus, A. Demortière, A. A. Franco, *J. Power Sources* **2023**, *554*, 232294.
- [45] Y. Chen, J. Jang, J. A. S. Oh, S. Ham, H. Yang, D. Lee, M. Vicencio, J. B. Lee, D. H. S. Tan, M. Chouchane, A. Cronk, M. Song, Y. Yin, J. Qian, Z. Chen, Y. S. Meng, *Adv. Energy Mater.* **2024**, *14*, 1.
- [46] Z. Siroma, T. Sato, T. Takeuchi, R. Nagai, A. Ota, T. Ioroi, *J. Power Sources* **2016**, *316*, 215.
- [47] S. Ohno, T. Bernges, J. Buchheim, M. Duchardt, A. K. Hatz, M. A. Kraft, H. Kwak, A. L. Santhosha, Z. Liu, N. Minafra, F. Tsuji, A. Sakuda, R. Schlem, S. Xiong, Z. Zhang, P. Adelhelm, H. Chen, A. Hayashi, Y. S. Jung, B. V. Lotsch, B. Roling, N. M. Vargas-Barbosa, W. G. Zeier, *ACS Energy Lett.* **2020**, *5*, 910.
- [48] A. Torayev, A. Rucci, P. C. M. M. Magusin, A. Demortière, V. De Andrade, C. P. Grey, C. Merlet, A. A. Franco, *J. Phys. Chem. Lett.* **2018**, *9*, 791.
- [49] D. Weitze, F. M. Zanotto, D. Z. Dominguez, A. A. Franco, *Energy Storage Mater.* **2024**, 103747.

Manuscript received: November 7, 2024

Revised manuscript received: November 12, 2024

Accepted manuscript online: November 12, 2024

Version of record online: December 23, 2024
